ADVANCED ELECTRONIC MATERIALS
www.advelectronicmat.de



# Cation Size Effects on the Electronic and Structural Properties of Solution-Processed In–X–O Thin Films

*Jeremy Smith, Li Zeng, Rabi Khanal, Katie Stallings, Antonio Facchetti,* Julia E. Medvedeva,* Michael J. Bedzyk,* and Tobin J. Marks**

**The nature of charge transport and local structure are investigated in amorphous indium oxide-based thin films fabricated by spin-coating. The In–X–O series where X = Sc, Y, or La is investigated to understand the effects of varying both the X cation ionic radius (0.89–1.17 Å) and the film processing temperature (250–300 °C). Larger cations in particular are found to be very effective amorphosizers and enable the study of high mobility (up to 9.7 $cm^2 V^{-1} s^{-1}$) amorphous oxide semiconductors without complex processing. Electron mobilities as a function of temperature and gate voltage are measured in thin-film transistors, while X-ray absorption spectroscopy and ab initio molecular dynamics simulations are used to probe local atomic structure. It is found that trap-limited conduction and percolation-type conduction mechanisms convincingly model transport for low- and high-temperature processed films, respectively. Increased cation size leads to increased broadening of the tail states (10–23 meV) and increased percolation barrier heights (24–55 meV) in the two cases. For the first time in the amorphous In–X–O system, such effects can be explained by local structural changes in the films, including decreased In–O and In–M (M = In, X) coordination numbers, increased bond length disorder, and changes in the $MO_x$ polyhedra interconnectivity.**

## 1. Introduction

In the past decade amorphous metal oxides (AMOs) have become attractive contenders as semiconducting and conducting materials for thin-film electronics.[1] There is a major driving force for applications based on optoelectronic device production using large-area, roll-to-roll processing methods enabled by mechanical flexibility and low-cost fabrication.[2] These include, but are by no means limited to, display backplanes, smart windows, solar cells, and radio-frequency identification tags. A combination of high carrier mobility, even in the amorphous state, excellent optical transparency, and the ability to process these thin-film materials from solution offers the potential of novel applications and a paradigm shift away from current technologies such as those based on amorphous silicon (a-Si). AMOs have recently achieved industrial prominence, with amorphous indium–gallium–zinc oxide (a-IGZO) for optical displays being a key example.[3] Typically, for both conducting and semiconducting electronic components, indium and/or zinc-based oxides are heavily doped with secondary cations such as Ga,[1a] Y,[4] Cd,[5] or Sn.[6] These transition and post-transition metal ions with large spherical *ns*-orbitals ($n \geq 4$) provide the dispersive conduction band required for electron transport, even in the amorphous phase.[7] In general, the secondary metal cations also affect several important film properties such as the degree of crystallinity, the local lattice structure, the formation of defects, as well as the electronic structure.[8] Furthermore, such cations are almost always necessary to control the film charge carrier concentration and to disrupt the lattice crystallinity, thus generating the amorphous phase. Therefore, deeper understanding of the role of these cations will be necessary to design future oxide systems with tailored properties.

Dr. J. Smith, L. Zeng, K. Stallings, Prof. A. Facchetti, Prof. T. J. Marks
Department of Chemistry and Materials Research Center
Northwestern University
Evanston, IL 60208, USA
E-mail: a-facchetti@northwestern.edu; t-marks@northwestern.edu
L. Zeng
Graduate Program in Applied Physics
Northwestern University
Evanston, IL 60208, USA
R. Khanal, Prof. J. E. Medvedeva
Department of Physics
Missouri University of Science and Technology
Rolla, MO 65409, USA
E-mail: juliaem@mst.edu

DOI: 10.1002/aelm.201500146

Prof. A. Facchetti
Polyera Corporation
8045 Lamon Avenue, Skokie, IL 60077, USA
Prof. M. J. Bedzyk
Department of Materials Science and Engineering and Materials Research Center
Northwestern University
Evanston, IL 60208, USA
E-mail: bedzyk@northwestern.edu

© 2015 WILEY-VCH Verlag GmbH & Co. KGaA, Weinheim

High-performance AMO films are typically grown by chemical vapor deposition,[9] physical vapor deposition such as sputtering and pulsed laser deposition,[1a] or by atomic layer deposition.[10] In these cases, the resulting thin film transistors (TFTs) have electron mobilities exceeding 10 $cm^2 V^{-1} s^{-1}$.[11] However, solution-based methods are attractive because of their roll-to-roll compatibility, reduced materials waste, and atmospheric pressure growth conditions. Additionally, it becomes possible to tune the oxide composition by simply changing the precursor solution composition in a straightforward and comprehensive fashion. Numerous oxide precursor routes have been developed, often based on sol–gel chemistry,[12] and generally high-temperature annealing steps (>400 °C) are required to remove impurities and achieve full oxide lattice condensation. Recently, several new methods have been reported that reduce processing temperatures.[13] Here we employ the "combustion" synthesis approach as developed in this laboratory,[13b] and previously applied to $In_2O_3$, In–Zn–O, In–Sn–O, In–Y–O, and In–X–Zn–O (X = Ga, Sc, Y, La) systems.[14] The precursor solution consists of an oxidizer in the form of the metal nitrate and a fuel (in this case acetylacetone), where, upon annealing at 250–300 °C, a rapid, highly exothermic and localized chemical reaction drives the formation of the metal oxide lattice/network, while not significantly increasing the film temperature. Combustion synthesis and other low-temperature routes allow complete conversion to the oxide in this temperature range but often result in device performance that varies with annealing temperature.[13]

The incorporation of secondary elements into the indium oxide lattice is expected to alter the local structure and lead to diminished long-range order. Furthermore, the composition dependence of the film crystallinity is predicted to differ for each added element due to the increased disorder induced by disparate cation sizes within the lattice. The chemical properties of $Sc^{3+}$, $Y^{3+}$, and $La^{3+}$ are similar, namely a 3+ oxidation state, octahedral coordination of oxygen around the metal in $M_2O_3$, and comparable oxide lattice enthalpies; however, their ionic radii $R_{ionic}(X)$ range from $0.95R_{ionic}(In^{3+})$ to $1.25R_{ionic}(In^{3+})$.[15] The size of the cation, which is determined by its electron configuration, will therefore be the dominant variable in this particular series and is expected to result in changes to the oxide properties. Consequently, in this contribution, we focus on the In–X–O system, where X = Sc, Y, La, with X concentrations varied between 2.5 and 12.5 at%, which crosses the crystalline-to-amorphous transition while maintaining complete oxide solid solution. We employ two processing temperatures, 250 and 300 °C, which for the In–X–O system, represent a "lower-quality" and "higher-quality" oxide film respectively, and which have noticeable differences in their structural and electronic properties.

The amorphous compositions are of particular interest from both a fundamental perspective and a technological one. Long-range order is absent, necessitating multiple relatively sophisticated techniques to elucidate structure–function relationships compared to crystalline semiconductors. X-ray absorption spectroscopy (XAS) analysis is one important method used to probe AMO materials on the ≈5 Å length scale and provides information on coordination number, average atomic separations, and atomic positional disorder of the different shells surrounding the central absorbing atom.[16] The XAS methods employed here are outlined in Sections 2.1 and 5. Computational modeling methods, specifically ab initio molecular dynamics (MD) simulations of the amorphous In–X–O lattices, are also employed, and it will be seen that they confirm the experimental trends. Since grain boundary defects are also largely suppressed in AMO materials, which is a significant factor influencing their electronic and mechanical properties, high electron mobilities can be achieved even by expeditious solution-processing methods. For example, this report demonstrates amorphous In–La–O (La: 5 at%) with $\mu_{FET}$ = 9.7 $cm^2 V^{-1} s^{-1}$. Furthermore, electron transport in In–X–O TFTs is characterized as a function of temperature in the range 150–300 K. It will be seen that these films exhibit thermally activated transport, and this can be associated with either trap-limited conduction for more disordered films, or percolation conduction for more ordered films (details of these models are provided in Section 2.3). Activation energies as a function of the X cation size are used to extract tail state distributions as well as conduction band potential barriers, and therefore provide a direct link between the electrical properties and the structural disorder induced by the secondary cation.

## 2. Structural and Electronic Characterization

### 2.1. X-Ray Absorption Spectroscopy

Due to large oxygen electronegativity, the structure of an amorphous oxide can be described as a network of $MO_x$ polyhedra where distortions and the connectivity of the polyhedra govern the transport properties. Therefore, it is crucial to investigate these structural characteristics in detail. For amorphous samples, which lack long-range order, XAS is an ideal technique complement to X-ray diffraction (XRD). XAS can be divided into two parts: X-ray absorption near-edge structure (XANES) which is indicative of the chemical state and site symmetry, and extended X-ray absorption fine structure (EXAFS), which can be analyzed quantitatively to obtain local structural information. The normalized linear EXAFS absorption coefficient $\chi(k)$ can be fitted by Equation (1)[16a]

$$\chi(k) = S_0^2 \sum_i \frac{N_i f_i(k)}{kR_i^2} \exp\left(-\frac{2R_i}{\lambda(k)}\right) \exp\left(-2k^2\sigma_{R_i}^2\right) \sin\left(2kR_i + \delta_i(k)\right) \quad (1)$$

where $S_0$ is the intrinsic loss factor, $\lambda(k)$ is the electron mean free path, $N_i$ and $R_i$ are the coordination number and bond distance of the $i$th shell of the absorbing atom, respectively, $f_i(k)$ and $\delta_i(k)$ are the backscattering amplitude and the phase shift, and $\exp(-2k^2\sigma_{R_i}^2)$ is the Debye–Waller factor—a measure of the structural disorder or the variation in $R_i$. The Fourier transformation of $\chi(k)$ generates a pseudo-radial distribution function ($p$-RDF) for the absorbing atom. For amorphous oxides we are interested in how the coordination number, bond distances, and the Debye–Waller factors change with processing temperature and choice of X cation.


© 2015 WILEY-VCH Verlag GmbH & Co. KGaA, Weinheim

### 2.2. Ab Initio Molecular Dynamics Simulation

The results of the EXAFS analysis can be compared to the local structure characteristics of amorphous oxides obtained from ab initio molecular dynamics (MD) simulations. The total, M–O, and M–M radial distribution functions are readily available from the MD models of amorphous oxide structures. Furthermore, an accurate comparison of the local (first-shell) structural characteristics in amorphous indium oxide (a-InO) and In–X–O materials can be made based on the average pair correlation function (Equation (2))[17]

$$R_{av} = \frac{\sum_i l_i \exp\left(1-(l_i/l_{min})^6\right)}{\sum_i \exp\left(1-(l_i/l_{min})^6\right)} \quad (2)$$

where $l_i$ and $l_{min}$ are individual metal–oxygen bond lengths and minimum bond length in the polyhedron, respectively. Using the pair correlation function $R_{av}$ the effective coordination number $N_{ECN}$ can be calculated for each polyhedron according to Equation (3)

$$N_{ECN} = \sum_i \exp\left(1-\left(l_i/R_{av}\right)^6\right) \quad (3)$$

We stress here that the above equations are used only to obtain the In–O and X–O first shell information; the wide distribution of the second-shell In–In and In–X distances makes the exponential fit in the $R_{av}$ and $N_{ECN}$ calculations inapplicable and a running coordination number $N_{RCN}$ is used instead. It is possible, however, to distinguish between the second and third shells using the optimized atomic coordinates of the MD simulated structures. For every In atom, the number of M (In or X) neighbors that share one, two, or three oxygen atoms with the central In can be determined, giving the average coordination number for corner, edge, or face-shared In–M, respectively. Then, the pair distribution functions, average distances, and statistical spreads can be found for edge- and corner-shared In–In pairs separately.[18]

Once a satisfactory agreement between the EXAFS and MD results for the structural properties as a function of cation size is obtained, the electronic structure of amorphous In–X–O materials is calculated. The ab initio nature of the MD simulations (density-functional equations are solved at every step during the MD quench) allows us to accurately describe the electronic states, defects, and the orbital character of all cations ($5s^0$ for In vs $(n-1)d^0ns^0$ for Sc, Y, or La) even during the quench. As such, our ab initio MD approach differs from a classical MD simulation, commonly employed to obtain amorphous oxide structures: the classical approach cannot describe the electronic localization and defects.

To analyze the localized states in the band gap and near the band edges, the inverse participation ratio (IPR) of an orbital $\psi_n(\vec{r}_i)$ can be found from ab initio density-functional calculations according to Equation (4), where $N$ is the number of volume elements in the cell and $i$ is the index of the volume element

$$\mathrm{IPR}(\psi_n) = N \frac{\sum_{i=1}^{N} \left|\psi_n(\vec{r}_i)\right|^4}{\left|\sum_{i=1}^{N} \left|\psi_n(\vec{r}_i)\right|^2\right|^2} \quad (4)$$

### 2.3. Thin Film Transistor Charge Transport Models

Charge transport in AMO semiconductors has been widely studied, both by TFT and Hall effect measurements. In general, amorphous semiconductors possess tail states that extend into the band gap close to the conduction band edge as a result of energetic disorder, as well as lower energy states arising from a variety of defects.[1d] For example, in metal oxides there is evidence for subgap states,[19] which can result in effects such as persistent photoconductivity[20] and bias instability.[21] The AMO density of tail states is usually much less than that of amorphous silicon due to the more isotropic nature of the s-orbital derived conduction band. Additionally, it has been found that carriers can percolate between potential barriers at the conduction band edge. Generally, there exists the possibility for charge transport by Mott variable range hopping (VRH) through localized states,[1d] as well as transport by carriers in extended states above the mobility edge $E_m$, either by trap limited conduction (TLC) or percolation conduction (PC).[22] VRH gives rise to a characteristic $1/T^{1/4}$ mobility relationship while TLC models can be described by a simple Boltzmann expression ($1/T$). The Kamiya–Nomura[23] PC model based on work by Adler et al.[24] assumes a Gaussian distribution of potential barriers attributed to the secondary cation; in the present case X, for the In–X–O system. This model ignores VRH because there is no evidence for the Hall voltage sign anomaly in AMO semiconductors but reproduces the apparent $1/T^{1/4}$ behavior at low temperature. Note, however, that Germs et al. argue that this is in fact a result of tail state VRH combined with band transport rather than PC.[25]

For n-type TFT operation the Fermi level $E_F$ moves toward the conduction band edge as the gate voltage $V_G$ is increased to more positive values. The ratio of free ($n_f$) to trapped ($n_{tr}$) charge carriers is, therefore, a function of $V_G$ as well as temperature and the density of tail states. For most amorphous semiconductors, a linearly increasing $V_T$ is observed with decreasing temperature as carriers are thermally generated from localized states, which in the case of a-IGZO has been shown to be ionization of oxygen vacancies.[8c] It is also well known that as the gate field is increased, $E_F$ moves toward the mobility edge $E_m$ and reaches the tail states at around $V_G - V_T = 0$. The percolation voltage $V_p$ is then defined as the point at which carriers can begin to move through extended states ($E_F \approx E_m$); however, the exact transition from TLC to PC dominated conduction is not abrupt. At higher voltages still, band transport may be feasible and the mobility becomes temperature independent. In this study, the focus is on relatively high-temperature measurements ($300 \geq T \geq 150$ K) and effective mobilities $\mu_{EFF}$ are extracted in the linear regime ($V_D << V_G$) for $V_G > V_T$. Therefore, a combination of TLC and PC models can be applied while assuming negligible VRH in this regime. The mobilities in each of these limits are given by Equations (5) and (6), respectively,


© 2015 WILEY-VCH Verlag GmbH & Co. KGaA, Weinheim

$$\mu_{\mathrm{TLC}} = \mu_0 A^* \left[ \frac{C_i \left( V_{\mathrm{G}} - V_{\mathrm{T}} \right)}{q N_{\mathrm{tr}}^0} \right]^{\frac{T_0}{T} - 1} \tag{5}$$

$$\mu_{\mathrm{PC}} = \mu_0 \exp\left( -\frac{q\varphi_{\mathrm{B}}}{kT} + \frac{\left(q\sigma_{\mathrm{B}}\right)^2}{2\left(kT\right)^2} \right) B^* \left( V_{\mathrm{G}} - V_{\mathrm{p}} \right)^{\alpha} \tag{6}$$

where $\mu_0$ is the band mobility, $A^*$ and $B^*$ are constants that depend on the density of conduction band states, $C_i$ is the dielectric geometric capacitance, $N_{\mathrm{tr}}{}^0$ is the areal density of tail states, $kT_0$ is the width of the tail state distribution, $\varphi_{\mathrm{B}}$ is the percolation barrier height, $\sigma_{\mathrm{B}}$ is the variation in $\varphi_{\mathrm{B}}$ assuming a Gaussian distribution of barriers, and $\alpha$ is related to the spatial coherence ratio of the barriers. The constant $\alpha$ depends on the spatial barrier width $W_{\mathrm{B}}$ and separation $D_{\mathrm{B}}$ and is given by $\alpha = 4(D_{\mathrm{B}} - W_{\mathrm{B}})/D_{\mathrm{B}}$. In both of these limiting cases, an activation energy $E_{\mathrm{A}}$ can be extracted from the slope of the Arrhenius plot and is given by Equation (7)

$$E_{\mathrm{A}}(V_{\mathrm{G}}) = -k \frac{\partial \ln(\mu)}{\partial(1/T)} = \begin{cases} kT_0 \ln\left( \dfrac{qN_{\mathrm{tr}}^0}{C_i} \right) - kT_0 \ln(V_{\mathrm{G}} - V_{\mathrm{T}}) & \text{for TLC} \\ q\varphi_{\mathrm{B}} - \dfrac{\left(q\sigma_{\mathrm{B}}\right)^2}{kT} & \text{for PC} \end{cases} \tag{7}$$

As can be seen here, the activation energy will be independent of $V_{\mathrm{G}}$ for the PC case, and be inversely related for the TLC case. Therefore by analyzing $E_{\mathrm{A}}$ as a function of $\ln(V_{\mathrm{G}} - V_{\mathrm{T}})$ as well as $\mu$ as a function of $(V_{\mathrm{G}} - V_{\mathrm{T,p}})$, the relative importance of TLC versus PC can be estimated, and the relevant physical parameters, $N_{\mathrm{tr}}$, $kT_0$, and $q\varphi_{\mathrm{B}}$ can be extracted.

## 3. Results and Discussion

The processing temperature $T_{\mathrm{a}}$ and the choice of X cation have a strong influence on the degree of crystallinity $\chi_{\mathrm{c}}$ of the final oxide film as shown in **Figure 1**. In the case of X = Sc at $T_{\mathrm{a}}$ = 300 °C all films are crystalline as estimated from the XRD peak areas ($\chi_{\mathrm{c}} > 0.90$). Note that moving to larger cations drastically reduces the crystallinity with In–Y–O showing a transition to the amorphous phase between 5 and 7.5 at% Y and In–La–O between 2.5 and 5 at% La. At $T_{\mathrm{a}}$ = 250 °C, most compositions are amorphous with the exception of 2.5 at% Sc which has a crystallinity of around $\chi_{\mathrm{c}} = 0.15$. Some films, for both processing temperatures, exhibit partial crystallinity ($\chi_{\mathrm{c}} < 0.15$) in the vicinity of the transition composition. As a control sample, an $In_2O_3$ film processed at $T_{\mathrm{a}}$ = 450 °C had a crystallinity of $\chi_{\mathrm{c}} > 0.98$. Despite differences in crystallinity, there is no significant difference in r.m.s surface roughness between these films as measured by AFM, which is found to be on average ≈0.17 nm. This demonstrates that: (i) differences in back surface roughness will not affect our electrical measurements, and (ii) even when crystalline, these films do no exhibit large grains or prominent grain boundaries.

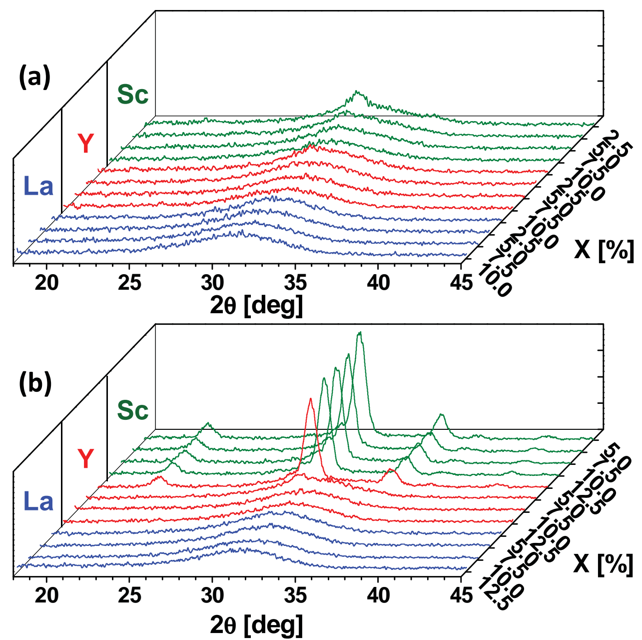


**Figure 1.** Grazing incidence XRD scans for In–X–O thin films processed at a) $T_{\mathrm{a}}$ = 250 °C and b) $T_{\mathrm{a}}$ = 300 °C. Film compositions are given as at% of the secondary cation, X (X = Sc, Y, La). Peak positions for the crystalline samples are at $2\theta$ = 21.7°, 30.8°, 35.7° and are consistent with the $In_2O_3$ bixbyite structure. The broad amorphous peak is centered at $2\theta$ = 29–33°.

In accord with the observed reduction in crystallinity with the X ionic size, ab initio MD simulations of amorphous In–X–O reveal that the number of $InO_6$ polyhedra varies with X: it is largest for X = Sc and notably smaller for X = Y or La (**Figure 2**). Moreover, in In–Sc–O the $InO_6$ polyhedra are mostly connected via edge sharing, resulting in the formation of large $InO_6$ clusters. The appearance of such clusters signifies the nucleation of $In_2O_3$ nanocrystallites, as was observed for a–InO.[18] In marked contrast to In–Sc–O, the $InO_6$ polyhedra in amorphous In–Y–O and In–La–O are distributed uniformly throughout the cell with a few polyhedra connected via edge- or corner sharing. This highlights the effectiveness of the larger cations such as Y or La in achieving amorphous In-based oxide structures.

The TFT properties at room temperature for all compositions and processing temperatures are shown in **Figure 3** and typical transfer and output curves are plotted in the Supporting Information. We will first distinguish between compositions that are measured to be amorphous by XRD ($\chi_{\mathrm{c}} = 0$) and those that are crystalline or partially crystalline ($\chi_{\mathrm{c}} > 0$). For $\chi_{\mathrm{c}} = 0$, the maximum electron mobilities are measured to be 9.7 and 5.1 $\mathrm{cm^2\ V^{-1}\ s^{-1}}$ for $T_{\mathrm{a}}$ = 300 and 250 °C, respectively, and are obtained in the In–La–O system. It is important to note that the use of X = La provides the highest performance amorphous films, since the large cation can be introduced into the system at relatively low concentrations, thus minimizing impurity scattering while still realizing the amorphous state. This approach, therefore, provides a useful strategy to readily introduce amorphous character into otherwise easily crystallizable materials. However, it should be noted that when considering all films, for a fixed X concentration, the general trend is that mobility decreases with increasing cation size similar to the previously

 © 2015 WILEY-VCH Verlag GmbH & Co. KGaA, Weinheim 

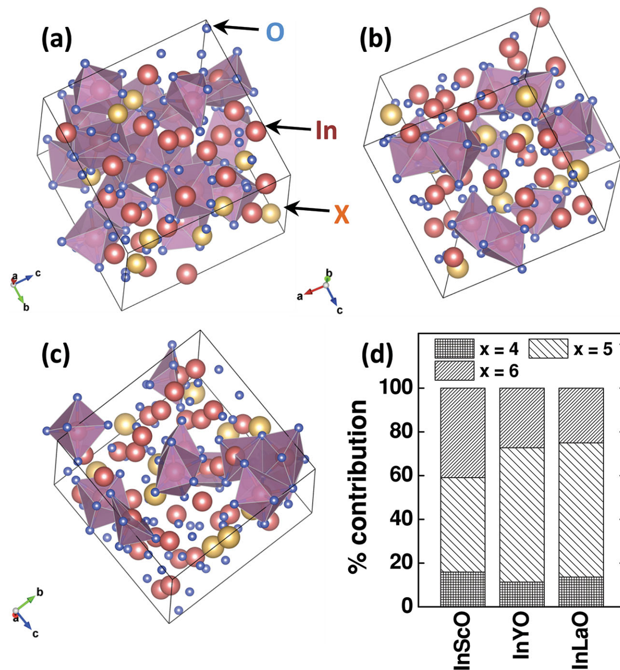


**Figure 2.** Representative structures of a) In–Sc–O, b) In–Y–O, and c) In–La–O from ab initio MD simulation. In each case, 20% of the In atoms are replaced with the secondary cation, X. $InO_6$ polyhedra are indicated on the structures in purple with In represented as red spheres, X as yellow spheres, and O as blue spheres. The proportion of $InO_x$ polyhedra with $x$ = 4, 5, and 6 are shown in d).

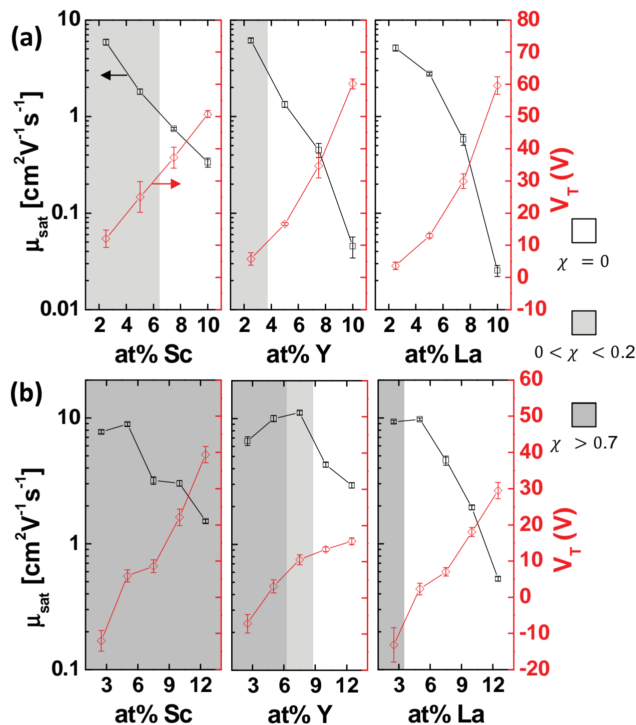


**Figure 3.** Thin film transistor data for measurements at room temperature taken in saturation to extract values of $\mu_{sat}$ and $V_T$. Regions corresponding to crystalline, semicrystalline, and amorphous films are indicated for films processed at a) $T_a$ = 250 °C and b) $T_a$ = 300 °C. Optimal devices characteristics are around 5 and 10 at% doping for the low and high-temperature processed films, respectively.

reported In–X–Zn–O system.[14] The crystalline ($\chi_c$ > 0.7) and partially crystalline (0 < $\chi_c$ < 0.15) samples typically exhibit good TFT characteristics ($\mu$ = 1–10 cm$^2$ V$^{-1}$ s$^{-1}$), however, tend to be slightly more inconsistent in their device parameters, often having negative (and less controllable) threshold voltages, and more variability between devices in subthreshold behavior, especially in cases of low X content. This result highlights the fact that although In–Y–O and In–Sc–O may have higher electron mobilities than In–La–O for a given X concentration, their increased propensity to crystallize can, especially in this case, be disadvantageous, and motivates the more detailed study of the electrical and local structure properties presented herein.

For all In–X–O films, increasing X concentration lowers $\mu$ and increases $V_T$. Especially at $T_a$ = 250 °C, this effect is decidedly detrimental for X concentrations above 7.5 at% since significant charge is trapped within localized states arising from the structural disorder. To further quantify the effects of this disorder, as well as that of the cation size, on the electron transport within the film, TFT parameters were measured as a function of temperature in the range 300 ≥ $T$ ≥ 150 K. Samples with 10 at% X at $T_a$ = 300 °C and 5 at% X at $T_a$ = 250 °C were chosen to provide optimal device operation and encompass a range of structural differences (see the Supporting Information for TFT characteristics). Typical Arrhenius plots for the In–La–O films are shown in **Figure** 4a,c. Linear fits at various values of $V_G$–$V_T$ yield the activation energies plotted in Figure 4b,d. There is a significant difference between films with 250 and 300 °C processing temperatures $T_a$. The former appear to be dominated by a TLC mechanism, whereas the latter have a much weaker dependence of the activation energy on the gate voltage, thus implying a PC dominated mechanism (Equation (7). In all cases, there is no strong dependence of $E_A$ on temperature, suggesting that the barrier height distribution $\sigma_B$ is very small. This is reasonable considering that these films only have two distinct cations unlike more complex oxides such as a-IGZO. From the present data, it is, therefore, possible to extract both tail state distributions ($N_{tr}^0$ and $kT_0$) from the $T_a$ = 250 °C films, and the approximate percolation barrier heights ($q\varphi_B$) from the $T_a$ = 300 °C films; these parameters are summarized in **Table 1**. Note that $kT_0$ is comparable to $kT$ and therefore a purely TLC model is not appropriate. However, the advantage of the activation energy analysis is that the effects of TLC and PC can be separated by their $V_G$ dependence, and therefore an estimate of $kT_0$ can be made even for small values. For larger $R_{ionic}$(X), increased structural disorder broadens the tail state distribution while the overall areal density of trap states at $E_m$ remains approximately constant. The DFT-calculated inverse participation ratios (IPR) for the MD-simulated nonstoichiometric amorphous In–X–O structures illustrate the existence of localized states within the band gap and near the band edges. These results support the broadening of the localized state distribution with the ionic size: a significant contribution from the localized states is found below, below and at, or below and above the Fermi level for X = Sc, Y, or La, respectively (full IPR data can be found in the Supporting Information).

 © 2015 WILEY-VCH Verlag GmbH & Co. KGaA, Weinheim 

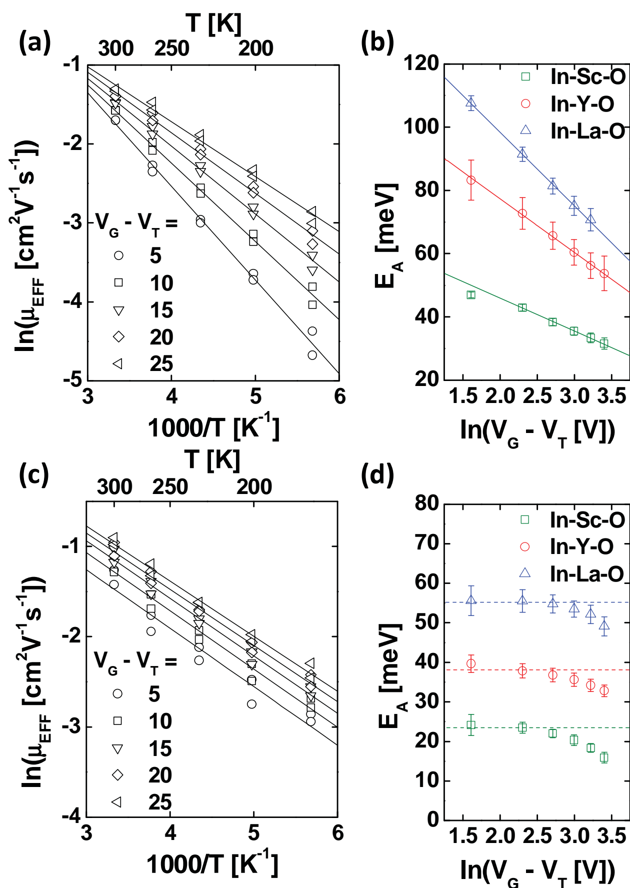


Figure 4. Temperature-dependent field-effect electron mobility showing linear fits for the extraction of the activation energy, $E_A$. Effective linear mobility is plotted for values of $V_G - V_T$ between 5 and 25 V for the In–La–O case with a) $T_a = 250$ °C and c) $T_a = 300$ °C. The extracted values of $E_A$ are plotted as a function of $\ln(V_G - V_T)$ for each film and at processing temperatures of b) $T_a = 250$ °C and d) $T_a = 300$ °C. Linear fits are made to the $T_a = 250$ °C data while the lines through the $T_a = 300$ °C data are guides to the eye.

For the more structurally ordered films that show percolation behavior, $\varphi_B$ also increases with increasing $R_{ionic}$(X). It has been suggested previously[22b] that percolation can arise due to secondary cations perturbing the conduction band, which is primarily derived from the In s-states. Here, we are able to show,

Table 1. Model fit parameters for the TFT measurements calculated from Equation (7).

| | $T_a$ [°C] | $kT_0$ [meV] | $N_{tr}^0$ [cm$^{-2}$] | $q\varphi_B$ [meV] | Dominant mechanism$^{a)}$ |
|---|---|---|---|---|---|
| In–Sc–O | 250 | 10 | $\approx 4 \times 10^{13}$ | – | TLC |
| In–Y–O | 250 | 17 | $\approx 5 \times 10^{13}$ | – | TLC |
| In–La–O | 250 | 23 | $\approx 4 \times 10^{13}$ | – | TLC |
| In–Sc–O | 300 | – | – | 24 | PC |
| In–Y–O | 300 | – | – | 38 | PC |
| In–La–O | 300 | – | – | 55 | PC |

$^{a)}$Mechanisms: TLC = trap-limited conduction; PC = percolation conduction.

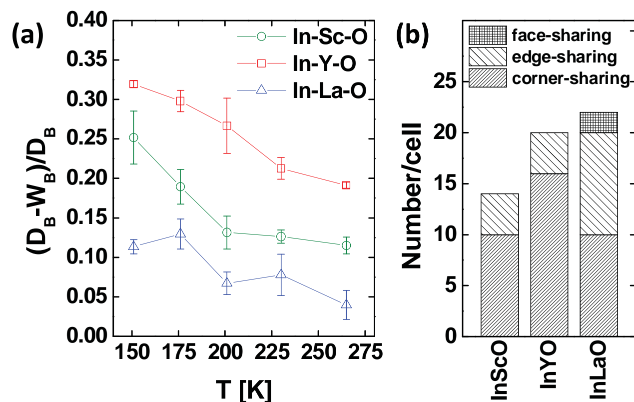


Figure 5. a) Values of the spatial coherence ratio calculated by fitting Equation (6) to the gate voltage dependence of the In–X–O electron mobility at temperatures between 150 and 275 K. b) Sharing statistics for $XO_x$ polyhedra as calculated from MD simulations of the structures. Numbers of corner-, edge-, and face-sharing polyhedra are shown per computational cell.

for the first time, a direct relationship between the measured potential barrier and the radius of the secondary cation, thus supporting this model. Values of the spatial coherence ratio for the potential barriers $(D_B - W_B)/D_B$ are also extracted from the $V_G$ dependence of the mobility (**Figure 5**a) and vary from 0.04 to 0.32, with the largest ratio observed in In–Y–O. Furthermore, a trend in the spatial distribution of $XO_x$ polyhedra within the amorphous cell is clearly observed in the results of the MD simulations (Figure 5b). In the In–Sc–O series, the $ScO_x$ polyhedra are connected primarily via corner sharing; several $ScO_x$ polyhedra stand separate from each other, i.e., remain disconnected. In In–Y–O, the number of corner-shared $YO_x$ polyhedra increases substantially, leading to the formation of long chains spread over the cell—in agreement with the observed largest spatial coherence ratio. In In–La–O, the large ionic radius of La as well as its tendency for over-coordination leads to formation of clusters of $LaO_x$ polyhedra more than half of which are connected via edge- or even face-sharing. Such $LaO_x$ clustering may be connected with the observed large potential barrier in amorphous In–La–O and the resulting TFT mobility decrease for larger La contents. At the same time, the observed spatial coherence ratios have some dependence on temperature suggesting that a purely PC model is inadequate for these materials, which is consistent with the deviation of $E_A$ from a constant in Figure 4d. While alternatives to PC descriptions have been proposed,[25] additional studies will be required before the current models for charge transport in amorphous metal oxide TFTs can be refined.

From the present TFT transport data, it is clear that two variables are especially important in these solution-processed In–X–O films: (i) the processing temperature, which strongly affects the charge transport mechanism; and (ii) the identity of the secondary cation, which influences both the tail state distribution and the percolation barriers. XAS is used here to further elucidate the nature of the structural disorder as seen in the electrical characterization.

Film XANES data at the In, Sc, Y, and La edges align well with their powder references (see the Supporting Information).


© 2015 WILEY-VCH Verlag GmbH & Co. KGaA, Weinheim

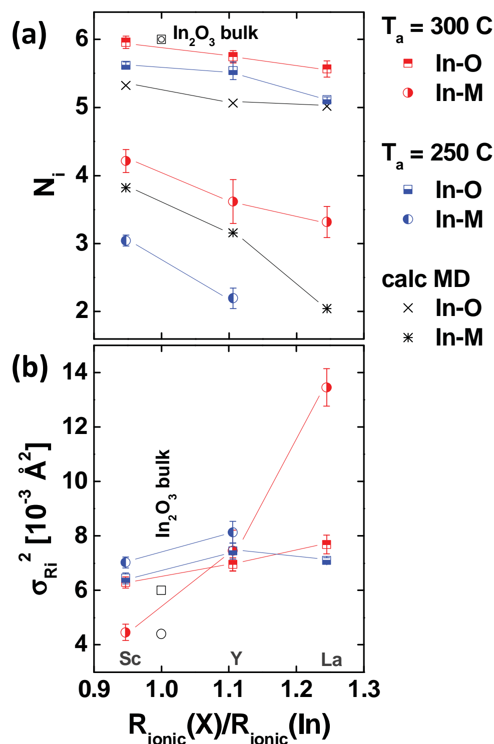


**Figure 6.** Fitting parameters from the In–X–O EXAFS measurements and ab initio MD simulations plotted as a function of the ionic radius of the X cation normalized to the radius of $In^{3+}$. a) The change in coordination number, $N$, for both the In–O and In–M (M = In or X) shells. b) The same for the change in Debye–Waller factor coefficient, $\sigma^2_{R_i}$.

Combined with the XPS peak positions, all metal ions maintain the 3+ oxidation state in the films after the combustion process. A more quantitative analysis from the EXAFS region provides the coordination number $N_i$ and Debye–Waller coefficient $\sigma^2_{R_i}$ for the first In–O shell and the first In–M shell (M = In or X), as shown in **Figure 6**, and the fitting results presented in **Table 2**. For all films, the calculated radii $R_i$ are relatively constant at 2.16 Å for the In–O shell and 3.36 Å for the In–M shell, which are comparable to the radii for crystalline $In_2O_3$ reference powder samples. The reductions in peak intensities in the p-RDF, especially for shells beyond the first In–M, correspond to a decrease in the coordination number and increased Debye–Waller factor in these shells, which are commonly seen as films become semicrystalline or amorphous. As the size of the secondary cation, X, increases $N_i$ decreases, whereas $\sigma^2_{R_i}$ increases. This effect is much more pronounced for the In–M shell, suggesting that $InO_x$ polyhedra remain relatively intact in the amorphous structure while disorder arises from distortions to the polyhedra network, i.e., to their interconnectivity. When comparing films annealed at 250 and 300 °C, the lower processing temperature leads to a greater drop in In–M coordination number—between 2.1 and 3.0 at $T_a$ = 250 °C versus 3.3 and 4.2 at $T_a$ = 300 °C. We can thus conclude that the introduction of larger secondary cations and/or lowering the processing temperature increases the amorphous network disorder, moving further away from the crystalline structure. In particular for the most amorphous samples, the "EXAFS-free" case is approached where all shells beyond the first In–O have very low intensities. This renders extraction of a unique In–M coordination number and Debye–Waller coefficient impossible in the In–La–O case with $T_a$ = 250 °C. Note that the effect of the 50 °C change in $T_a$ is greater than moving from X = Sc to X = La. This may partially explain the different transport mechanisms (PC and TLC) observed in the transistor measurements.

The ab initio MD simulations for the In–X–O systems support the coordination number and bond length variations seen in the EXAFS experiments. For the first In–O or X–O shell, the calculated effective coordination numbers $N_{ECN}$s and bond lengths $R_{av}$s are summarized in **Table 3**. These values are in agreement with EXAFS showing: (i) a slight contraction in the In–O coordination number as the X cation size is increased and (ii) nearly invariant In–O bond lengths. For comparison, the average In–O distance and In–O coordination number in a-InO

**Table 3.** Structural characteristics of the first In–O and X–O shell as obtained from the ab initio MD simulations. The average coordination $N_{ECN}$ and average distance $R_{av}$ parameters were calculated according to Equations (2) and (3).

| | $N_{ECN}$(In–O) | $R_{av}$(In–O) [Å] | $N_{ECN}$(X–O) | $R_{av}$(X–O) [Å] |
|---|---|---|---|---|
| In–Sc–O | 5.32 | 2.158 | 5.23 | 2.068 |
| In–Y–O | 5.06 | 2.142 | 6.01 | 2.273 |
| In–La–O | 5.02 | 2.154 | 6.56 | 2.451 |

**Table 2.** EXAFS fitting parameters for the first In–O and In–M (M = In or X) shells calculated using Equation (1).

| | $T_a$ [°C] | $N_i$ | | $R_i$ [Å] | | $\sigma^2_{R_i}$ [$10^{-3}$ Å$^2$] | |
|---|---|---|---|---|---|---|---|
| | | In–O | In–M | In–O | In–M | In–O | In–M |
| In–Sc–O | 250 | 5.62 | 3.04 | 2.152 | 3.358 | 6.45 | 7.02 |
| In–Y–O | 250 | 5.54 | 2.20 | 2.151 | 3.316 | 7.45 | 8.13 |
| In–La–O | 250 | 5.11 | 2.4[a] | 2.156 | 3.340 | 7.10 | 9[a] |
| In–Sc–O | 300 | 5.95 | 4.21 | 2.166 | 3.363 | 6.29 | 4.46 |
| In–Y–O | 300 | 5.75 | 3.62 | 2.155 | 3.365 | 6.96 | 7.46 |
| In–La–O | 300 | 5.56 | 3.32 | 2.147 | 3.368 | 7.69 | 13.5 |

[a]Shells beyond the first have very low intensity (approaching EXAFS-free amorphous); therefore, the coordination number and Debye–Waller factor for the second shell cannot be uniquely fitted.


© 2015 WILEY-VCH Verlag GmbH & Co. KGaA, Weinheim

obtained from MD simulations are 2.16 Å and 5.0, respectively. Although the In–O local structure characteristics show little sensitivity to the X cation size, the $N_{ECN}$ and $R_{av}$ values for X–O vary significantly among X, as expected from the strong X–O bonds. The average X–O distances in amorphous In–X–O nearly match the corresponding natural X–O distances, i.e., those found in the respective crystalline $X_2O_3$ materials. The average effective coordination $N_{ECN}$ increases as the cation size increases, with Sc and La being under- and over-coordinated with O atoms, respectively, whereas the Y atoms retain the natural coordination number of 6.

As noted in Section 2.2, Equations (2) and (3) are not applicable for the second shell and beyond owing to broad In–M distance distributions. Instead, the total In–M coordination or a running coordination number $N_{RCN}$ is calculated as a function of the radial distance $r$ from an In atom. The $N_{RCN}$ values for both In–O and In–M shells, **Figure 7**a,b, respectively, decrease with increasing cation size, but the effect is far more pronounced for the In–M shell. At $r = 3.35$ Å, which corresponds to the edge-shared In–In distance in crystalline $In_2O_3$, $N_{RCN}$(In–M) decreases from 3.82 to 3.16 to 2.05 for Sc to Y to La, respectively. In a-InO, the calculated $N_{RCN}$(In–In) is 2.69. Accordingly, the average distance between In and X connected via edge-sharing (second shell) increases with X ionic size: from 3.08 to 3.36 Å to 3.52 Å for In–Sc to In–Y to In–La, respectively. For comparison, the average edge-shared In–In distances are less affected, increasing from 3.26 to 3.31 Å for Sc and Y to La, respectively. Although it is impossible to directly compare these numbers to the experimental EXAFS data, which are derived from solution-processed films rather than a melt-and-quench simulation, it is evident that these numbers correlate well with those in Figure 6 and follow the same trend. The increased second shell (In–M) bond distances can contribute to a larger effective mass; however, the spatial distribution and interconnection of the $InO_x$ and $XO_x$ polyhedra are expected to play the key role in determining the electron mobility in these amorphous oxides.

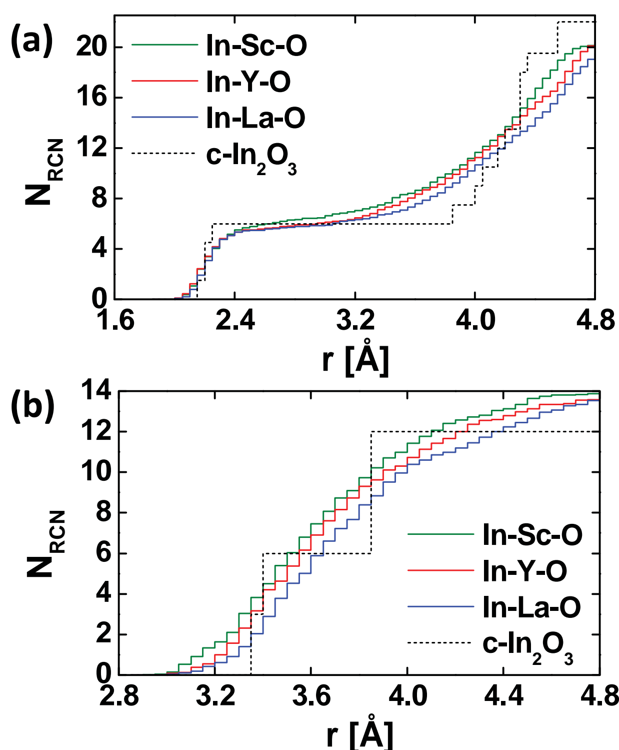


**Figure 7.** Ab initio MD simulation results for the In–X–O systems showing the calculated running coordination number, $N_{RCN}$. The radius $r$ is the distance from the central In atom with a) showing the In–O coordination and b) showing the In–M coordination (where M = In or X). Crystalline $In_2O_3$ values are also shown for reference.

In addition to local disorder, the strength and type of M–O bonding have been shown to be good indicators of electron transport properties since weakly bound oxygen or oxygen not fully coordinated by a metal ion can introduce trap states and reduce the mobility and bias-stress stability in TFTs.[26] Previous work in this laboratory on oxygen "getter" effects in In–X–Zn–O materials suggests this may also be relevant to the In–X–O system.[14] XPS measurements were therefore carried out, focusing on the O1s peak, deconvoluting it into a M–O–M peak, a M–O(H) peak, and a weakly bound M–O–R surface peak (**Figure 8**a,b). The ratio of M–O–M peak area to total peak area $\eta_{M-O-M}$ is shown in Figure 8c and represents the fraction of oxygen in the film that is completely incorporated into the metal oxide lattice. Additionally, using the ratio of O1s peaks to the In 3d, Sc 2p, Y 3d, or La 3d peaks allows estimation of the In–X–O film stoichiometry, which indicates that the oxide films preserve the precursor solution stoichiometry. All films, independent of the processing temperature or composition, are found to be close to stoichiometric (60 at% O). However, it is evident that $\eta_{M-O-M}$ is a function of the processing temperature. For the $T_a = 300$ °C case, the oxide is well formed and $\eta_{M-O-M}$ is relatively unaffected by the secondary cation since the thermal energy at this processing temperature allows good relaxation of the oxide lattice. However, $\eta_{M-O-M}$ is lower for all compositions processed at $T_a = 250$ °C, suggesting that the oxide film is more defective, leading to the change from charge transport being limited by percolation in the conduction band to trapping and detrapping from tail states. Additionally, the larger cations tend to reduce $\eta_{M-O-M}$ further, unlike in the high-temperature case, which is consistent with the broadening of the density of tail states at $T_a = 250$ °C when changing from Sc to Y to La.

## 4. Conclusions

The incorporation of the Group 3/4f cations Sc, Y, and La into indium oxide thin films by straightforward solution-processing techniques at low temperatures provides important information about the structural and electronic properties of amorphous oxide semiconductors. First and importantly, to facilitate the study of these systems, note that these elements can be introduced without the need for complex processing equipment and over a wide compositional range. It is found that large values of the X ionic radius $R_{ionic}$(X) compared to indium, such as when X = La, can induce the amorphous state even at relatively low X concentrations, resulting in thin films with high electron mobilities. The effect of the cation size and processing temperature on the electron transport mechanism was also investigated here, and found to be dominated by trap-limited conduction

 © 2015 WILEY-VCH Verlag GmbH & Co. KGaA, Weinheim 

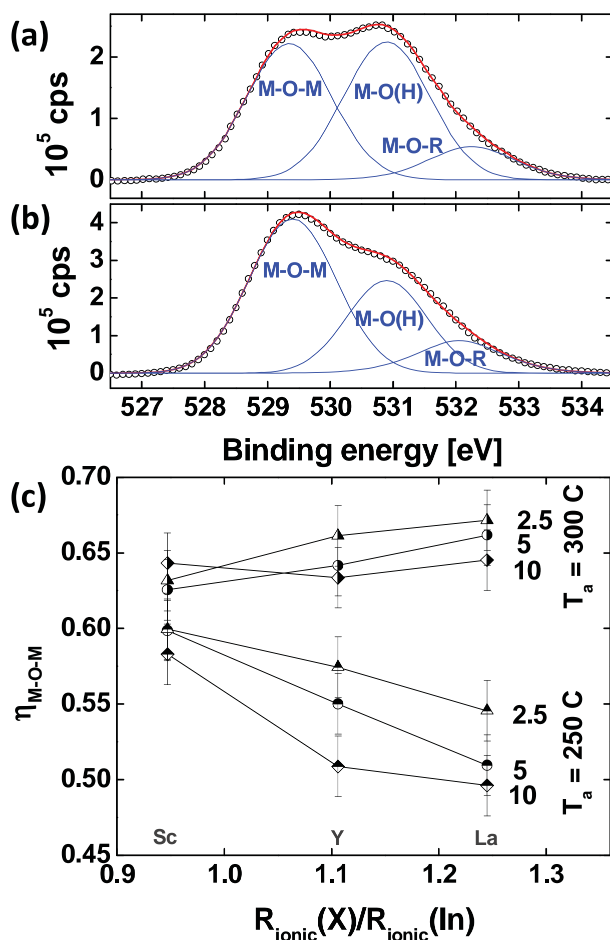


**Figure 8.** Fitting of the O1s XPS peaks for a 10 at% In–La–O film processed at a) $T_a$ = 250 °C and b) $T_a$ = 300 °C. Peak positions were fixed and correspond to fully bound oxygen (M–O–M), partially bound oxygen (M–O(H)) and weakly bound oxygen at the surface or organic impurities (M–O–R). c) The ratio of M–O–M peak area to total area, $\eta_{M-O-M}$, is plotted as a function of the X cation size for compositions of 2.5, 5, and 10 at%.

(TLC) at low processing temperatures. This contrasts markedly with the high-temperature processed films, where activation energies for transport are much lower and independent of TFT gate voltages, suggesting transport dominated by electrons above the conduction band edge—in this case the conduction can be modeled using the typical Kamiya–Nomura percolation expression. It is observed in the TLC case that the tail state trap distribution broadens as the ionic radius of X increases for a fixed X concentration. In the percolation case, it is found that larger ionic radii increase the potential barrier height, suggesting that disruptions to the indium oxide lattice by the introduction of the secondary cation X are the cause of such barriers. To understand the origin of this phenomenon, the local structure and valence of the oxide films were investigated using XAS and XPS and also compared to ab initio molecular dynamics simulations of the In–X–O system. A decrease in In–O and In–M coordination numbers is observed as the X cation size increases from that of $In^{3+}$. The fall in coordination number from the ideal crystalline value of 6 is especially apparent for the first In–M shell and for larger cation sizes (i.e., X = La). This result is concurrent with an increase in the variation of In–O and In–M shell bond distance, although the average distances remain constant. The interconnectivity of the $MO_x$ polyhedra and structural disorder are therefore determined to be the main origins of the tail state width and percolation barrier height changes, and demonstrates that local structure measurements are vital to understanding charge transport in amorphous oxide electronics.

## 5. Experimental Section

*Oxide Precursor Solutions*: Solutions were prepared by dissolving $M(NO_3)_3$ in 2-methoxyethanol (M = In, Sc, Y, or La, 0.05 mol $L^{-1}$, 10 mL) and adding acetylacetone (32 µL) and $NH_{3(aq)}$ (30 µL). Solutions were stirred for 16 h before mixing in the desired ratios. The solutions were then filtered through a 0.2 µm Teflon filter, spin-coated at 3500 $s^{-1}$ for 30 s and annealed at 250 or 300 °C ($T_a$) in air for 15 min yielding ≈5 nm thick oxide films. Repeated spin-coating and annealing was used to build up thicker films. This gave more dense oxide films than a single thick layer due to porosity caused by gas evolution during solution processing. The chosen thickness gave us optimal device performance. Hotplate surface temperatures were controlled to ±2 °C and only very small changes in substrate temperature were seen during film combustion. Changes in local temperature within the film during growth were extremely difficult to quantify accurately but were common to all solution-processing techniques. Generally in these films, heat energy generated from chemical reactions will either be consumed driving lattice/network formation or will be dissipated relatively rapidly due to the large surface area-to-volume ratio. $T_a$ therefore defines the technologically relevant thermal budget for the process. Films for TFTs were fabricated on heavily doped silicon wafers with 300 nm of thermal oxide (four repeated layers of combustion oxide, film thickness ≈15 nm). Films for grazing incidence XRD studies were fabricated on silicon wafers (four layers), and films for XAS were fabricated on fused-quartz substrates (11 layers, X: 10 at%). A postanneal in clean dry air at $T_a$ was carried out at <5% relative humidity on all films.

*Thin-Film Transistors*: TFTs were fabricated by patterning the In–X–O films with oxalic acid to reduce gate leakage, followed by evaporation of aluminum source-drain contacts through a shadow mask. Device dimensions were $L$ = 50 µm, $W$ = 1 mm. Electrical measurements were carried out either in air or a vacuum probe station (<5 × $10^{-6}$ mbar) with an Agilent B1500A parameter analyzer. Transfer characteristics were measured in both the linear and saturation regimes of the TFT. Samples for low-temperature measurements were mounted on an Advanced Research Systems liquid nitrogen cryostat controlled by a Lake Shore 331 temperature controller. Mobilities were extracted in the range of $V_G$–$V_T$ between 5 and 25 V where leakage currents were always >10× lower than the source-drain current. Effective mobility $\mu_{EFF}$ was calculated in the linear regime ($V_D$ = 5 V) using Equation (8) and choosing appropriate onset voltages $V_{on}$ estimated from the transfer characteristics. This method gave an average mobility for both trapped and untrapped electrons and correctly represented the gate voltage dependence of the mobility.[1e]

$$\mu_{EFF}(V_G) = \frac{L}{WC_i}\frac{I_D(V_G)}{V_D(V_G - V_{on})} \tag{8}$$

*X-Ray Absorption Spectroscopy*: Experiments were conducted at sector 5BMD of the Advanced Photon Source of Argonne National Laboratory (ANL). A Si(111) double crystal monochromator was used to produce a 12 mm (horizontal) by 1 mm (vertical) beam. The incident beam energies were tuned to near the In, Sc, Y K-edge and La L-edge (27.940, 4.492, 17.038, 6.266 keV, respectively) to measure XAS spectra at the above four edges. Films were placed 45° from the incident direction, and data


© 2015 WILEY-VCH Verlag GmbH & Co. KGaA, Weinheim

were collected in fluorescence mode using a four-element silicon drift detector (SII NanoTechnology). The reference powders were uniformly spread on Scotch tape (3M Corp.) and measured in transmission mode using an ionization chamber (Oxford-Danfysik). EXAFS spectra were extracted and normalized using ATHENA software packages.[27] The intrinsic loss factor ($S_0^2$ = 1.06) for fitting the indium K-edge was obtained by modeling of the reference powders for each absorbing atom, and kept fixed when fitting the film data. The bond distances, coordination numbers, and Debye–Waller factors were obtained by the FEFF simulations using a cluster of the bixbyite structure with a radius of 6 Å centered on the absorbing atom. All the normalized absorption coefficients $\chi(k)$ were Fourier transformed using a Hanning window over the specified $k$-range and fit in $k$-space with $k$-weight 3.

*Ab Initio Molecular Dynamics Simulation*: The amorphous In–X–O structures were generated using first-principles MD as implemented in the Vienna Ab initio Simulation package (VASP).[28] The calculations were based on density functional theory within generalized gradient approximation (GGA) with the PBE functional.[29] For the initial structure, a bixbyite $In_2O_3$ cell containing 130 atoms ($In_{52}O_{78}$) and a density of 7.116 g cm$^{-3}$ was used. For ternary structures, 20% of In atoms in crystalline $In_2O_3$ were replaced by metal X (Sc, Y, or La) resulting in the stoichiometric structure $In_{44}X_{10}O_{81}$; the cell volume was adjusted to maintain the density in the In-based samples. Also, amorphous nonstoichiometric $In_{44}X_{11}O_{77}$ structures were modeled by removing oxygen atoms in the initial structures, i.e., prior to liquid quench process. The amorphous In–O and In–X–O structures were then obtained using the liquid-quench approach as follows. First, to remove any crystalline memory, each initial structure was melted at 3000 K for 6 ps. The melt was then cooled to 1700 K at the rate of 100 K/1.2 ps, and then rapidly quenched to 100 K at the rate of 200 K/1.2 ps. In order to make the calculations computationally efficient, a cutoff of 260 eV was used and the $k$-point sampling was restricted to $k$-point only during melting and quenching processes. Finally, the structures were equilibrated at 300 K for 6 ps with a cut-off energy of 400 eV. All simulations were carried out within NVT ensemble with Nose–Hoover thermostat using integration time step of 2 fs.

*Structural Characterization*: Grazing incidence XRD was carried out on a Rigaku ATX-G workstation (Cu K$\alpha$, $\lambda$ = 1.541 Å) with an incidence angle, $\alpha = 0.5°$ compared to a critical angle for $In_2O_3$ of $\alpha_C = 0.37°$. After background subtraction, the degree of crystallinity $\chi_c$ was estimated from the ratio of area under the crystalline peaks (after subtracting the amorphous peak) to total area under the X-ray diffraction pattern. Diffraction peaks were fitted with a pseudo-Voigt function (Gaussian–Lorentzian product). Atomic force microscopy (AFM) was carried out in tapping mode on a Bruker ICON system. XPS was carried out on a Thermo Scientific ESCALAB 250Xi with O1s peaks being deconvoluted into separate peaks at 529.3, 530.9, and 532.1 eV.

## Supporting Information

Supporting Information is available from the Wiley Online Library or from the author.

## Acknowledgements

The authors acknowledge support from the Office of Naval Research (MURI N00014-11-1-0690; J.S., K.S.) and the Materials Research Center of Northwestern University (NSF-MRSEC DMR-1121262; R.K., L.Z.). This work made use of the J. B. Cohen X-Ray Diffraction Facility supported by the NSF-MRSEC program (DMR-1121262) at the MRC-NU. XAS measurements were carried out at the 5BMD beamline of the DuPont-Northwestern-Dow Collaboration Assess Team (DND-CAT) at the Advanced Photon Source (APS) of Argonne National Laboratory (ANL). This work also made use of the KECK-II and NIFTI facilities at Northwestern University's Atomic and Nanoscale Characterization Experimental Center (NUANCE) for XPS and AFM. NUANCE was supported by NSF-NSEC, NSF-MRSEC, Keck Foundation, the State of Illinois, and Northwestern University. The authors thank Prof. M. Grayson for insightful discussions. Computational resources were provided by the NSF-supported XSEDE program, Grant TG-DMR080007.

Received: April 28, 2015
Published online: June 5, 2015

[1] a) K. Nomura, H. Ohta, A. Takagi, T. Kamiya, M. Hirano, H. Hosono, *Nature* **2004**, *432*, 488; b) E. Fortunato, P. Barquinha, R. Martins, *Adv. Mater.* **2012**, *24*, 2945; c) S. Jeong, J. Moon, *J. Mater. Chem.* **2012**, *22*, 1243; d) N. F. Mott, E. A. Davis, *Electronic Processes in Non-Crystalline Materials*, Clarendon Press, Oxford **1979**; e) J. F. Wager, D. A. Keszler, R. E. Presley, *Transparent Electronics*, Springer, Berlin **2008**.
[2] S. R. Forrest, *Nature* **2004**, *428*, 911.
[3] IGZO oxide semiconductor mass produced by Sharp and Semiconductor Energy Laboratory Co. Ltd. for display technologies http://sharp-world.com/igzo/, accessed: October 2014.
[4] J. W. Hennek, M.-G. Kim, M. G. Kanatzidis, A. Facchetti, T. J. Marks, *J. Am. Chem. Soc.* **2012**, *134*, 9593.
[5] A. Wang, J. R. Babcock, N. L. Edleman, A. W. Metz, M. A. Lane, R. Asahi, V. P. Dravid, C. R. Kannewurf, A. J. Freeman, T. J. Marks, *Proc. Natl. Acad. Sci.* **2001**, *98*, 7113.
[6] H. Kim, C. M. Gilmore, A. Piqué, J. S. Horwitz, H. Mattoussi, H. Murata, Z. H. Kafafi, D. B. Chrisey, *J. Appl. Phys.* **1999**, *86*, 6451.
[7] O. N. Mryasov, A. J. Freeman, *Phys. Rev. B: Condens. Matter* **2001**, *64*, 233111.
[8] a) K. Nomura, T. Kamiya, H. Ohta, T. Uruga, M. Hirano, H. Hosono, *Phys. Rev. B: Condens. Matter* **2007**, *75*, 035212; b) A. U. Adler, T. C. Yeh, D. B. Buchholz, R. P. H. Chang, T. O. Mason, *Appl. Phys. Lett.* **2013**, *102*, 122103; c) H.-K. Noh, K. J. Chang, B. Ryu, W.-J. Lee, *Phys. Rev. B: Condens. Matter* **2011**, *84*, 115205.
[9] J. Ni, H. Yan, A. Wang, Y. Yang, C. L. Stern, A. W. Metz, S. Jin, L. Wang, T. J. Marks, J. R. Ireland, C. R. Kannewurf, *J. Am. Chem. Soc.* **2005**, *127*, 5613.
[10] J. Heo, S. Bok Kim, R. G. Gordon, *Appl. Phys. Lett.* **2012**, *101*, 113507.
[11] T. Kamiya, H. Hosono, *NPG Asia Mater.* **2010**, *2*, 15.
[12] S. R. Thomas, P. Pattanasattayavong, T. D. Anthopoulos, *Chem. Soc. Rev.* **2013**, *42*, 6910.
[13] a) K. K. Banger, Y. Yamashita, K. Mori, R. L. Peterson, T. Leedham, J. Rickard, H. Sirringhaus, *Nat. Mater.* **2011**, *10*, 45; b) M.-G. Kim, M. G. Kanatzidis, A. Facchetti, T. J. Marks, *Nat. Mater.* **2011**, *10*, 382; c) Y. Hwan Hwang, J.-S. Seo, J. Moon Yun, H. Park, S. Yang, S.-H. Ko Park, B.-S. Bae, *NPG Asia Mater.* **2013**, *5*, e45; d) S. T. Meyers, J. T. Anderson, C. M. Hung, J. Thompson, J. F. Wager, D. A. Keszler, *J. Am. Chem. Soc.* **2008**, *130*, 17603; e) C.-H. Choi, S.-Y. Han, Y.-W. Su, Z. Fang, L.-Y. Lin, C.-C. Cheng, C.-H. Chang, *J. Mater. Chem. C* **2015**, *3*, 854; f) S. Jeong, J.-Y. Lee, S. S. Lee, Y. Choi, B.-H. Ryu, *J. Phys. Chem. C* **2011**, *115*, 11773.
[14] J. W. Hennek, J. Smith, A. Yan, M.-G. Kim, W. Zhao, V. P. Dravid, A. Facchetti, T. J. Marks, *J. Am. Chem. Soc.* **2013**, *135*, 10729.
[15] R. Shannon, *Acta Cryst.* **1976**, *A32*, 751.
[16] a) J. J. Rehr, R. C. Albers, *Rev. Mod. Phys.* **2000**, *72*, 621; b) D. E. Proffit, Q. Ma, D. B. Buchholz, R. P. H. Chang, M. J. Bedzyk, T. O. Mason, *J. Am. Ceramic Soc.* **2012**, *95*, 3657.
[17] a) R. Hoppe, *Angew. Chem. Int. Ed.* **1970**, *9*, 25; b) R. Hoppe, S. Voigt, H. Glaum, J. Kissel, H. P. Müller, K. Bernet, *J. Less Common Met.* **1989**, *156*, 105.
[18] D. B. Buchholz, Q. Ma, D. Alducin, A. Ponce, M. Yacaman, R. Khanal, J. E. Medvedeva, R. P. H. Chang, *Chem. Mater.* **2014**, *26*, 5401.


© 2015 WILEY-VCH Verlag GmbH & Co. KGaA, Weinheim

[19] a) W. Körner, D. F. Urban, C. Elsässer, *J. Appl. Phys.* **2013**, *114*, 163704; b) S. Sallis, K. T. Butler, N. F. Quackenbush, D. S. Williams, M. Junda, D. A. Fischer, J. C. Woicik, N. J. Podraza, B. E. White, A. Walsh, L. F. J. Piper, *Appl. Phys. Lett.* **2014**, *104*, 232108.
[20] J. Robertson, Y. Guo, *Appl. Phys. Lett.* **2014**, *104*, 162102.
[21] J. F. Conley, *IEEE Trans. Device Mater. Rel.* **2010**, *10*, 460.
[22] a) S. Lee, K. Ghaffarzadeh, A. Nathan, J. Robertson, S. Jeon, C. Kim, I.-H. Song, U.-I. Chung, *Appl. Phys. Lett.* **2011**, *98*, 203508; b) K. Nomura, T. Kamiya, H. Ohta, K. Ueda, M. Hirano, H. Hosono, *Appl. Phys. Lett.* **2004**, *85*, 1993.
[23] T. Kamiya, K. Nomura, H. Hosono, *Appl. Phys. Lett.* **2010**, *96*, 122103.
[24] D. Adler, L. P. Flora, S. D. Senturia, *Solid State Commun.* **1973**, *12*, 9.
[25] W. C. Germs, W. H. Adriaans, A. K. Tripathi, W. S. C. Roelofs, B. Cobb, R. A. J. Janssen, G. H. Gelinck, M. Kemerink, *Phys. Rev. B: Condens. Matter* **2012**, *86*, 155319.
[26] J. G. Um, M. Mativenga, J. Jang, *Appl. Phys. Lett.* **2013**, *103*, 033501.
[27] B. Ravel, M. Newville, *J. Synchrotron Radiat.* **2005**, *12*, 537.
[28] a) G. Kresse, J. Hafner, *Phys. Rev. B: Condens. Matter* **1993**, *47*, 558; b) G. Kresse, J. Hafner, *Phys. Rev. B: Condens. Matter* **1994**, *49*, 14251; c) G. Kresse, J. Furthmüller, *Phys. Rev. B: Condens. Matter* **1996**, *54*, 11169; d) G. Kresse, J. Furthmüller, *Comput. Mater. Sci.* **1996**, *6*, 15.
[29] J. P. Perdew, K. Burke, M. Ernzerhof, *Phys. Rev. Lett.* **1996**, *77*, 3865.


© 2015 WILEY-VCH Verlag GmbH & Co. KGaA, Weinheim